

On the Origin of the Dramatic Spectral Variability of WPVS 007

Junyao Li,^{1,2*} Mouyuan Sun,^{1,2†} Tinggui Wang,^{1,2} Zhicheng He^{1,2} and Yongquan Xue^{1,2‡}

¹CAS Key Laboratory for Research in Galaxies and Cosmology, Department of Astronomy, University of Science and Technology of China, Hefei 230026, China

²School of Astronomy and Space Science, University of Science and Technology of China, Hefei 230026, China

Accepted XXX. Received YYY; in original form ZZZ

ABSTRACT

We report the discovery of large-amplitude mid-infrared variabilities (MIR; ~ 0.3 mag) in the *Wide-field Infrared Survey Explorer* W1 and W2 bands of the low-luminosity narrow-line Seyfert 1 galaxy WPVS 007, which exhibits prominent and varying broad-absorption lines (BALs) with blueshifted velocity up to ~ 14000 km s⁻¹. The observed significant MIR variability, the UV to optical color variabilities in the *Swift* bands that deviate from the predictions of pure dust attenuation models, and the fact that *Swift* light curves can be well fitted by the stochastic AGN variability model suggest that its observed flux variabilities in UV-optical-MIR bands should be intrinsic, rather than owing to variable dust extinction. Furthermore, the variations of BAL features (i.e., trough strength and maximum velocity) and continuum luminosity are concordant. Therefore, we propose that the BAL variability observed in WPVS 007 is likely induced by the intrinsic ionizing continuum variation, alternative to the rotating-torus model proposed in a previous work. The BAL gas in WPVS 007 might be in the low-ionization state as traced by its weak N V BAL feature; as the ionizing continuum strengthens, the C IV and Si IV column densities also increase, resulting in stronger BALs and the emergence of high-velocity components of the outflow. The outflow launch radius might be as small as $\sim 8 \times 10^{-4}$ pc under the assumption of being radiatively driven, but a large-scale origin (e.g., torus) cannot be fully excluded because of the unknown effects from additional factors, e.g., the magnetic field.

Key words: galaxies: active — galaxies: individual (WPVS 007) — quasars: absorption lines.

1 INTRODUCTION

Outflows are commonly observed in active galactic nuclei (AGNs; e.g., Tombesi et al. 2010; Gofford et al. 2013; Harrison et al. 2014), which are possibly driven by radiation pressure (e.g., Proga et al. 2000; Proga & Kallman 2004), magnetic field (e.g., Ohsuga et al. 2009; Jiang et al. 2014), or Compton heating (e.g., Begelman et al. 1983) from the accretion disk. Powerful outflows can be identified via blueshifted broad-absorption lines (BALs; FWHM > 2000 km s⁻¹) in either UV or X-ray bands, and are believed as an important candidate for AGN feedback by injecting their kinetic energy and momentum outward (see, e.g., Fabian 2012 and King & Pounds 2015 for reviews). However, direct measurements of outflow geometry, distance, stability, energy and hence its

influence on galaxy environment and evolution are so far inconclusive. Multi-epoch observations and variability studies that focus on sources with prominent outflow features provide a new way to constrain these properties, and thus help shed light on how and where the winds are launched, accelerated, varied, and coupled with galactic-wide materials (e.g., FilizAk et al. 2012; Grier et al. 2015; Rogerson et al. 2016; Matzeu et al. 2017; Parker et al. 2017; McGraw et al. 2018; Pinto et al. 2018; DeCicco et al. 2018).

Previous studies have found that two mechanisms are mainly responsible for the observed BAL variability: (1) changes in the ionization state; and (2) changes of the covering factor (e.g., the absorbers moving into/out-of the sight-line). The first mechanism can easily explain the coordinated relationships between BALs and continuum variabilities found in large quasar samples (e.g., Wang et al. 2015; He et al. 2017); and the variability timescale, which provides important information of the recombination timescale, can be used to constrain crucial outflow properties such as gas

* E-mail: lijunyao@mail.ustc.edu.cn

† E-mail: ericsun@ustc.edu.cn

‡ E-mail: xuey@ustc.edu.cn

density, outflow distance and mass outflow rate (e.g., [Gofford et al. 2014](#); [He et al. 2019](#)). While in the second scenario, the cloud transverse motion (thus BAL variability) is expected to be independent of the continuum, and the variability (transverse) timescale can be used to constrain the distance of the absorber (e.g., [Capellupo et al. 2012](#); [Matzeu et al. 2016](#); [Rogerson et al. 2016](#); [Braitto et al. 2018](#); [Matzeu et al. 2019](#)). Therefore, distinguishing different variability mechanisms is crucial for us to investigate the physical conditions of the outflow.

The low-luminosity ($M_V \approx -19.7$) narrow-line Seyfert 1 galaxy (NLS1) WPVS 007, located at $z = 0.02882$ ([Grupe et al. 1995](#)), is one of the most extensively studied source owing to its peculiar variability behavior (e.g., [Leighly et al. 2009](#); [Grupe et al. 2013](#); [Leighly et al. 2015](#)). At its first discovery in the *ROSAT* all-sky survey, it appeared as a bright X-ray source with an extremely soft spectrum ([Grupe et al. 1995](#)). However, in the subsequent observations by *Chandra* ([Vaughan et al. 2004](#)) and *Swift* observatories ([Grupe et al. 2007](#)), it showed persistently weak X-ray emission with no detections in most of the time, while the first hard X-ray detection suggested the existence of a high column-density ($N_{\text{H}} \sim 10^{22-23} \text{ cm}^{-2}$), partial-covering absorber ([Grupe et al. 2008](#)).

The spectroscopic monitoring by the *Hubble Space Telescope* (*HST*) and the *Far Ultraviolet Spectroscopic Explorer* (*FUSE*) also revealed some unique phenomena. In the 1996 *HST* observation, WPVS 007 only exhibited a mini-BAL with a maximum velocity $V_{\text{max}} \sim 900 \text{ km s}^{-1}$ ([Leighly et al. 2009](#)). However, a significant outflow feature traced by the blueshifted P v BAL with $V_{\text{max}} \sim 6000 \text{ km s}^{-1}$ appeared in the 2003 *FUSE* spectrum ([Leighly et al. 2009](#)), and a more dramatic C iv BAL with $V_{\text{max}} \sim 13000 \text{ km s}^{-1}$ was detected in the 2010 *HST* observation ([Leighly et al. 2015](#)). The discovery of these prominent outflow features makes the low-luminosity WPVS 007 a distinct object since powerful outflows are more likely to be found in luminous quasars (e.g., PDS 456; [Pounds et al. 2003](#); [Reeves et al. 2003](#); [Hamann et al. 2008](#); [Dunn et al. 2010](#); [Danekkar et al. 2018](#)). Interestingly, in the three succeeding *HST* observations from 2013 to 2015, the wind velocities decreased persistently down to a few thousand km s^{-1} , accompanied with dimming and reddening of the continuum ([Leighly et al. 2015](#)). The significant velocity “shifts” ([Leighly et al. 2015](#); also see our Section 4.2) make WPVS 007 an extraordinary object owing to the fact that most of observed BAL troughs only show variations in profile and strength rather than velocity structure (e.g., [Grier et al. 2016](#)).

The coordinated correlation between outflow velocity and continuum flux is usually unexpected in the moving cloud scenario. However, [Leighly et al. \(2015\)](#) (hereafter L15) proposed an interesting scenario that outflows are launched from an inhomogeneous rotating torus to explain the coordination. As the torus rotates, the scale height varies, the extinction changes, and outflows with different launching velocities move into our sightline, which result in both changes on continuum fluxes and outflow velocities, thus building the bridge between velocity and continuum variabilities (see their Figure 5 and Section 3.4). However, we note that the BAL strength is also correlated with continuum flux (see Section 4.1), but the physical reason behind such a relationship has not been explored yet.

In addition, L15 intensively analyzed the UV-optical photometries for WPVS 007 and captured a particular “occultation event” which lasted for ~ 60 days in 2015. By assuming Keplerian motion of the occulting cloud, they constrained the distance of the absorber to be at the torus scale, and explained the occultation as a result of variable reddening in the rotating torus framework (see their Figure 1 and Figure 5 and our Section 4.4). If variable reddening also governs the flux variability during the \sim ten-years *Swift* monitoring ([Grupe et al. 2013](#)), we should expect no significant mid-infrared (MIR) variability since the reprocessed MIR emission is insensitive to dust extinction.

However, we check the *Wide-field Infrared Survey Explorer* (*WISE*) data for this source and find large-amplitude variabilities ($\sim 0.3 \text{ mag}$) in *W1* ($3.4 \mu\text{m}$) and *W2* ($4.6 \mu\text{m}$) bands, suggesting that WPVS 007 must experience significant intrinsic luminosity variability. Although L15 can explain the occultation event in the variable extinction scenario, how the additional variable factor (i.e., the intrinsic luminosity) would influence our understanding of the dramatic BAL variability in this particular source is currently unclear. Therefore, in this work, we plan to extensively analyze the combined UV-optical-IR variabilities of WPVS 007 aiming at comprehensively exploring its long-term variability nature and the driving mechanism of its coordinated BAL variabilities, which might give important clues on constraining physical properties of this unique low-luminosity, NLS1-BAL system. This paper is organized as follows. In § 2 we describe the observations and data reduction. In § 3 we present our analyses on *WISE* variabilities, color variabilities and *Swift* light curves that lead us to the conclusion that the variable intrinsic luminosity is mainly responsible for the flux variabilities observed in WPVS 007, instead of variable extinction. In § 4 we discuss the origin of its dramatic BAL variability in the variable luminosity framework and put important constraints on the driving mechanism and launch radius of the varying outflows. The results are summarized in § 5. Throughout this paper, we adopt a flat cosmology with $H_0 = 70.0 \text{ km s}^{-1} \text{ Mpc}^{-1}$, $\Omega_{\text{M}} = 0.30$, and $\Omega_{\Lambda} = 0.70$.

2 OBSERVATIONS AND DATA REDUCTION

The archival *WISE* MIR photometries, *Swift* UV-optical photometries and *HST* UV-optical spectra used in this work are summarized in Table 1. Below we give a detailed description of each data set.

2.1 WISE observations

The *WISE* mission ([Wright et al. 2010](#)) and its successor, the *Near-Earth WISE Reactivation* (*NEOWISE*) mission ([Mainzer et al. 2014](#)), have imaged the full sky repeatedly since January 2010. The *WISE* light curves for WPVS 007 at *W1* and *W2* bands are extracted from the IRSA service¹ with a $2''$ matching radius. Data points with quality flags

¹ See <https://irsa.ipac.caltech.edu/Missions/wise.html>.

Table 1. Information of archival *WISE*, *Swift* and *HST* data used in this work

Telescope / Instrument	Observation Date	Photometric Bands / Spectral Coverages	PI
<i>WISE</i>	2010 May – 2016 Nov	<i>W1</i> (3.6 μm) and <i>W2</i> (4.5 μm)	<i>WISE</i>
<i>Swift</i> / XRT	2005 Oct – 2018 Mar	<i>UVW2</i> , <i>UVW1</i> , <i>UVM2</i> , <i>U</i> , <i>B</i> , <i>V</i>	<i>Swift</i> & Dirk Grupe
<i>HST</i> / FOS	1996 Jul	1140 \AA – 2508 \AA (BL) and 1573 \AA – 6872 \AA (RD)	Robert Goodrich
<i>HST</i> / COS	2010 Jun	1230 \AA – 2050 \AA (FUV) and 1700 \AA – 3200 \AA (NUV)	Karen Leighly
<i>HST</i> / COS	2013 Jun	1230 \AA – 2050 \AA (FUV) and 1700 \AA – 3200 \AA (NUV)	Karen Leighly
<i>HST</i> / COS	2013 Dec	1230 \AA – 2050 \AA (FUV) and 1700 \AA – 3200 \AA (NUV)	Karen Leighly
<i>HST</i> / COS	2015 Mar	1230 \AA – 2050 \AA (FUV) and 1700 \AA – 3200 \AA (NUV)	Karen Leighly
<i>HST</i> / COS	2017 Mar	1230 \AA – 2050 \AA (FUV) and 1700 \AA – 3200 \AA (NUV)	Karen Leighly

of $qi_fact < 1$, $saa_sep < 5$ and $moon_masked = 1$ are excluded.² The binned light curves are shown in Fig. 1 as orange (*W1*) and green (*W2*) triangles. The individual observations are shown in gray points.

2.2 *Swift* observations

WPVS 007 has been extensively monitored with *Swift* (Gehrels et al. 2004) using XRT and UVOT, including *UVW2*, *UVW1*, *UVM2*, *U*, *B* and *V* bands centered at 1928 \AA , 2246 \AA , 2600 \AA , 3465 \AA , 4392 \AA and 5468 \AA , respectively (e.g., Grupe et al. 2007, 2008, 2013). We extract its *Swift* light curves using the HEASOFT version 6.24 *uvmaghist* tool. The source region is selected using a circle with a radius of 5'' centered on the source and the corresponding background region is selected by an annulus with a 12.5'' inner radius and a 25.0'' outer radius. The binned *UVM2* light curve (in bins of 6 days) is displayed in Figure 1.

The intrinsic 1450 \AA luminosity (L_{1450}) is calculated by extrapolating the *UVW1* band and *U* band luminosities with a power law. The photometry used in the calculation has been corrected for Galactic reddening assuming $E(B - V) = 0.012$ mag (Schlegel et al. 1998) and the Cardelli et al. (1989) extinction law. L_{1450} is then converted into bolometric luminosity (L_{bol}) using $\log L_{\text{bol}} = (4.745 \pm 1.007) + (0.910 \pm 0.022) \log \lambda L_{1450}$ (Runnoe et al. 2012) and the resulting L_{bol} for the six *HST* observations (Section 2.3) are presented in Table 2. The *UVW1* and *U* bands are utilized here because they are relatively less affected by possible intrinsic extinction (owing to their longer wavelengths compared to the *UVM2* and *UVW2* bands; e.g., Calzetti et al. 2000) and emission lines (note that the *B* and *V* bands are close to strong emission lines; see Figure 2). Note that we mainly focus on the relative variability of luminosity in the following analysis. Therefore, we argue that the constant host galaxy contamination and a different bolometric conversion factor would not influence our main results materially.

2.3 *HST* observations

WPVS 007 has been observed six times by the Faint Object Spectrograph (FOS) or Cosmic Origins Spectrograph (COS) aboard *HST* since 1996 (see Table 1). The spectra are extracted from the *HST* online dataset³ that are calibrated and shown in Figure 2 after smoothing by averaging the adjacent seven pixels. The BAL regions of C IV, Si IV and N V are plotted in bottom panels. To obtain the BAL velocity, we fit the observed spectra by an empirical model. We model the continuum with a power law in line-free regions (1000–1430 \AA , 1470–1610 \AA , 1620–1680 \AA , 1740–1760 \AA and 1850–2900 \AA). The absorption features are fitted using a set of Gaussian profiles. The emission lines are modeled with Lorentz profiles except for the 2015 spectrum for which we use the Gaussian profile since the `curve_fit` python package we used is unable to find a solution with the Lorentz profile. The BAL troughs are determined as a combination of broad Gaussians, and the observed maximum velocity of the outflow is calculated as the velocity corresponding to the first point of the best fitted normalized BAL profiles which equals to 0.99 counted from the bluest wavelength. The derived velocities of WPVS 007 are summarized in Table 2 and the spectral fitting results of C IV and Si IV BAL regions are shown in Figure 3.

3 CHANGE OF OBSCURATION OR INTRINSIC LUMINOSITY?

3.1 *WISE* variability

MIR variability has been widely utilized as a powerful tool to distinguish various variability mechanisms. The AGN MIR emission in the *WISE* *W1* and *W2* bands is mainly produced by the hot dust re-radiation surrounding the central engine. Due to the small extinction in the MIR bands, large-amplitude MIR variability should only arise from intrinsic luminosity variability rather than the change of obscuration (Sheng et al. 2017; Stern et al. 2018). For WPVS 007 that exhibits ~ 0.3 mag variability in the *WISE* bands (see Figure 1), it would require a $\Delta A_V \sim 5$ change in extinction if a variable obscuration scenario is assumed, insensitive to the adopted extinction models (Cardelli et al. 1989; O'Donnell

² See https://wise2.ipac.caltech.edu/docs/release/allwise/expsup/sec3_2.html for details.

³ See <http://archive.stsci.edu/hstonline>.

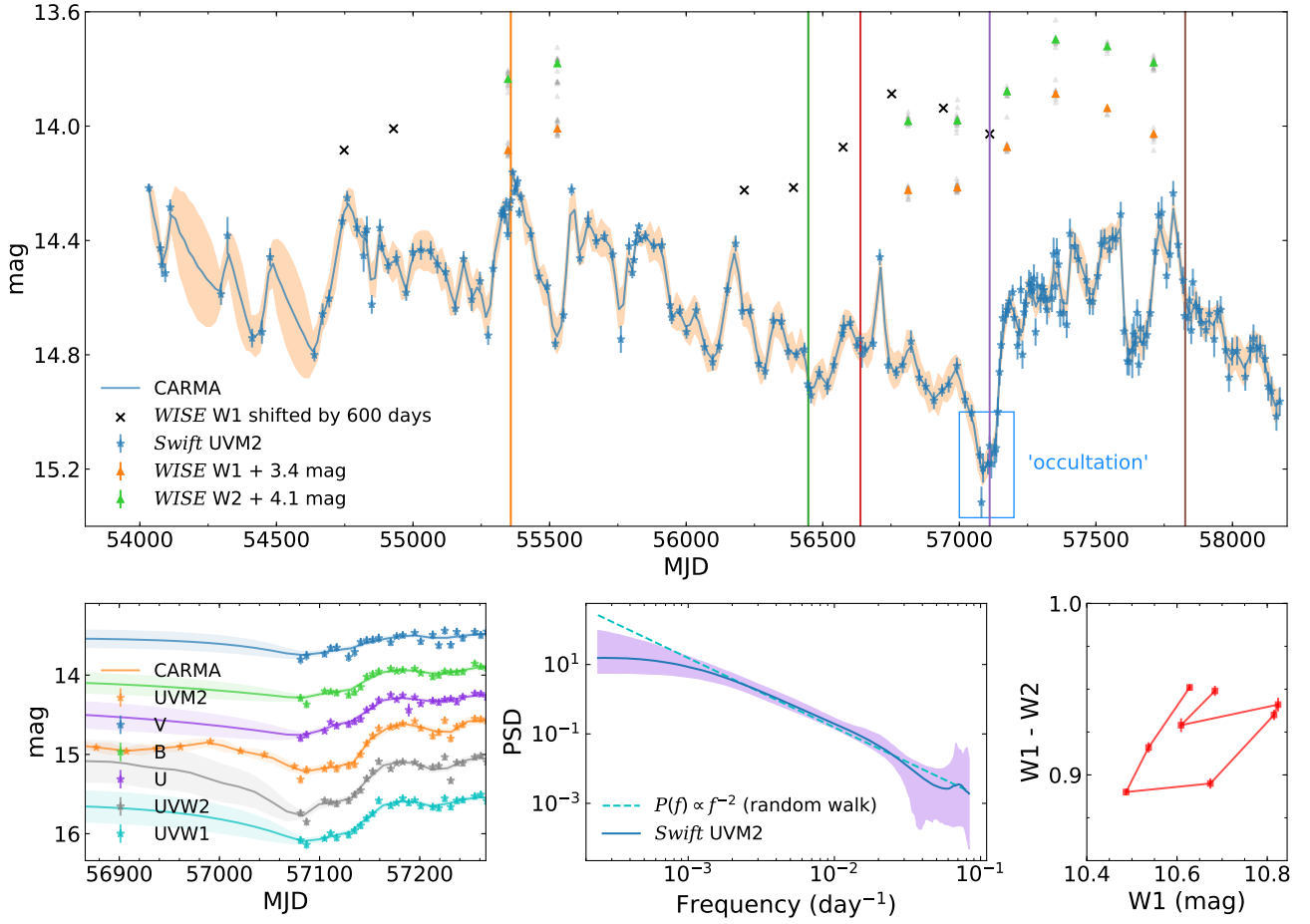


Figure 1. *Upper:* WISE and Swift light curves for WPVS 007. The time of five HST observations from 2010 to 2017 are labeled by solid lines. The WISE data have been artificially shifted vertically for demonstration purpose. The WISE W1 data corrected for light-crossing time lag (by simply shifting the light curve by 600 days, see Section 3.3) are shown in light blue. The UVM2 light curve is fitted by the CARMA code (Kelly et al. 2014) that models the AGN stochastic variability by a Gaussian continuous-time autoregressive process. The 1σ confidence interval of the fit is shown in shaded region. *Lower left:* Zoom-in of the “occultation event” reported in Leighly et al. 2015. The data have been artificially shifted vertically for demonstration purpose. *Lower middle:* The solid line and shaded area represent the PSD and the corresponding 1σ confidence region of the Swift UVM2 light curve derived from CARMA, respectively. The dashed line represents the PSD of the random walk model (i.e., $P(f) \propto f^{-2}$). *Lower right:* The W1 – W2 color as a function of W1 magnitude. The large WISE variability amplitude and its color variability suggest that the intrinsic luminosity must change. The Swift light curves including the occultation event (see Section 4.4) can be well fitted by the stochastic AGN variability model. The PSD for WPVS 007 has a high-frequency slope consistent with -2 , and flattens at low frequencies, in agreement with the damped random walk model (e.g., Kelly et al. 2009). These results suggest that the Swift variability pattern is consistent with intrinsic AGN stochastic variability.

Table 2. Broad-absorption line properties of WPVS 007 at the time of HST observations.

Date	L_{bol} (erg s ⁻¹)	C IV V_{max} (km s ⁻¹)	C IV EW (Å)	Si IV V_{max} (km s ⁻¹)	Si IV EW (Å)
1996 Jun	5.2×10^{43}	900 (N v)	–	–	–
2010 Jun	3.6×10^{44}	14100	20.4	11900	9.2
2013 Jun	1.8×10^{44}	9000	15.1	6700	8.8
2013 Dec	2.0×10^{44}	8700	15.9	6300	7.4
2015 Mar	1.4×10^{44}	7700	6.3	4000	3.3
2017 Mar	2.4×10^{44}	13400	19.2	5800	9.9

Note. The bolometric luminosity and mini-BAL velocity for the 1996 HST observation are adopted from Leighly et al. (2009) and Leighly et al. (2015), respectively.

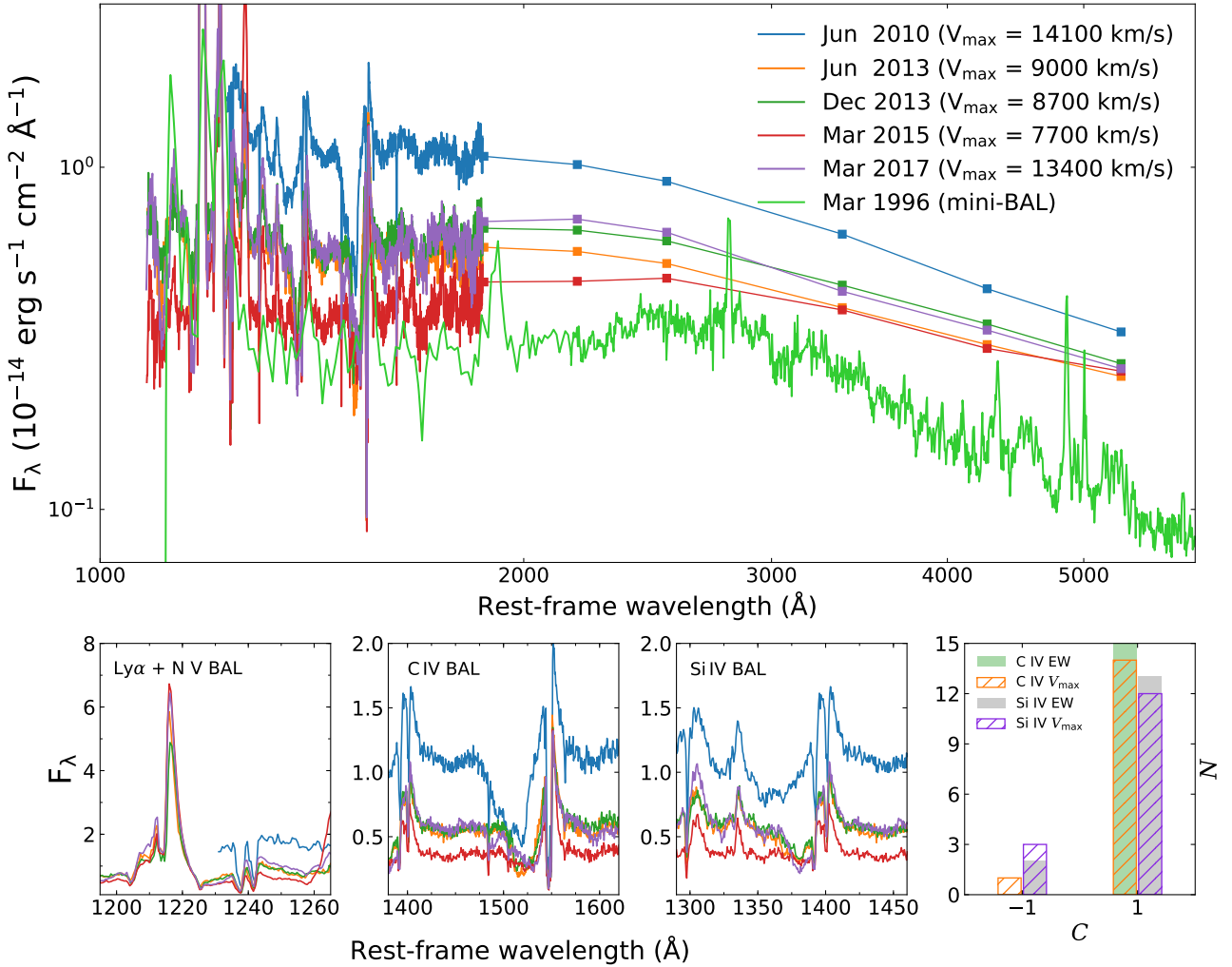


Figure 2. *Upper:* *HST* spectra from 1996 to 2017. The *Swift* photometries at the times of *HST* observations are shown as squares. *Lower left:* The regions of $\text{Ly}\alpha$, N v, C iv, and Si iv lines (The units are the same as the upper panel). *Lower right:* Distribution of concordance index C . C is assigned as +1/-1 if the outflow strength (velocity) and bolometric luminosity vary in the same/opposite sign. The C iv and Si iv BAL strength and velocity for most epochs vary coordinately with luminosity.

1994; Fitzpatrick 1999). This would transform into a ~ 5 mag change in the V band and $\sim 14 - 16$ mag change in the $UVM2$ band, which are all significantly larger than the true variability amplitudes during the *Swift* monitoring (i.e., only ~ 1 mag change at maximum). Moreover, we find that the $W1 - W2$ color generally increases with increasing $W1$ magnitude (see the inset in Figure 1), suggesting that the MIR color becomes redder when the source dims. This might be explained by that the torus temperature decreases with decreasing luminosity, thus the spectral energy distribution (SED) becomes redder in the faint state. Such a phenomenon is also unexpected if the UV-optical flux variabilities are dominated by the obscuring materials move into/out-of the sightline. Therefore, the MIR variability observed in WPVS 007 suggests that its intrinsic luminosity must vary significantly.

3.2 Color variability

As the intrinsic luminosity changes, the color would also change in response and is typically observed as being “bluer-when-brighter” that has been widely found in quasar variabilities (e.g., Ruan et al. 2014; Guo & Gu 2016), which could be well explained by the stochastic temperature fluctuation in an inhomogeneous accretion disk (e.g., Dexter & Agol 2011; Cai et al. 2016, 2018). Alternatively, the flux variability caused by variable extinction also displays a similar trend, since extinctions are more significant at shorter wavelengths (e.g., Calzetti et al. 2000).

To examine whether the color variability in WPVS 007 also requires the change of intrinsic luminosity, we divide *Swift* light curves into seven bins based on their $UVM2$ fluxes. The SEDs in each bin and their average values are shown in Figure 4, in which the bluer-when-brighter behavior can be clearly seen. If variable extinction governs the color variability, we should be able to reproduce

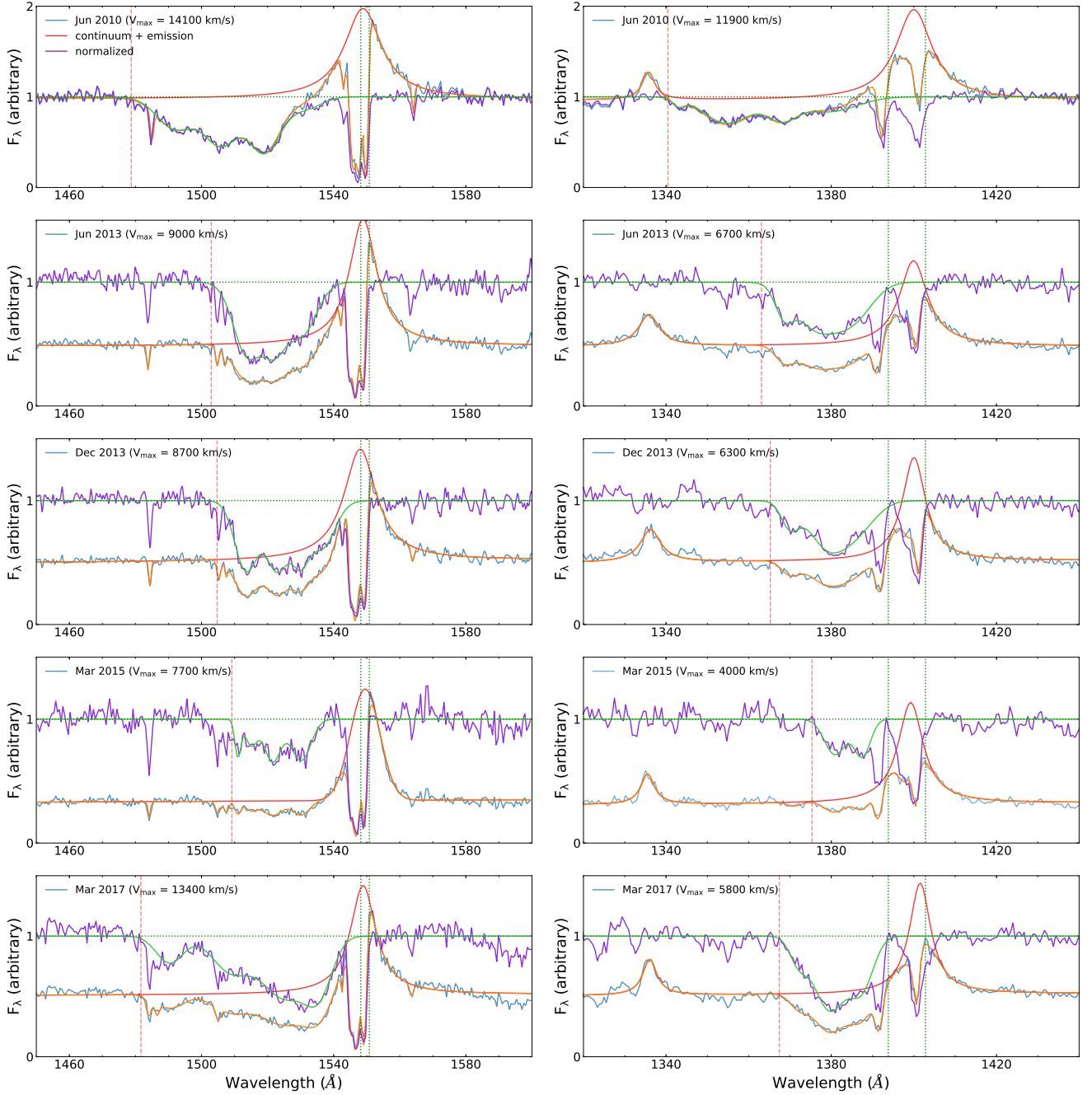


Figure 3. Spectral fitting results of C IV (left) and Si IV (right) BAL regions. The observed spectrum is shown in blue. The spectral fitting result is shown in orange. The best fit emission line plus continuum is shown in red. The purple curve represents the normalized spectrum. The normalized model-fitting BAL component is shown in green. The dotted lines at (1548.2 Å, 1550.8 Å) and (1398.8 Å, 1402.8 Å) represent the rest-frame wavelengths of C IV and Si IV doublets, respectively. The red vertical dashed line marks the position of the observed maximum outflow velocity defined in Section 2.3.

low-flux SEDs by simply adding dust extinction to high-flux SEDs. Note that L15 captured a particular occultation event lasting for ~ 60 days in 2015 and explained it as a result of variable extinction (but see Section 4.4). Since our *WISE* data cannot deny this possibility, we exclude the data during the occultation event while calculating the SEDs (but we note that adding them back does not affect our results).

We test various extinction models (Cardelli et al. 1989;

O'Donnell 1994; Fitzpatrick 1999; Gordon et al. 2003) and show the results of using the Milky Way (MW; Cardelli et al. 1989) and Small Magellanic Cloud (SMC; Gordon et al. 2003) extinction curves in Figure 4 for illustration. The top SED is extinguished using a range of A_V values from 0 to 0.3. For the resulting SEDs at given A_V values (shown as dotted curves) which match well with the observed SEDs at *B* and *U* bands, they all significantly underestimate the fluxes at *UVM2* and *UVW1* bands, insensitive on the assumed values

of $R_V = A_V/E(B - V)$. Note that we do not consider the $UVW2$ band here since it might be contaminated by the C III] emission line. This result suggests that the variable extinction model fails to reproduce the bluer-when-brighter trend, and intrinsic variability is required to account for the observed color variability of WPVS 007.

3.3 *Swift* variability

As discussed in Sections 3.1 and 3.2, the intrinsic luminosity of WPVS 007 must vary significantly to account for the long-term *WISE* and UV to optical color variations, and the change of obscuration may play a subordinate role. If our model is correct, we should be able to explain the flux variations in UV-optical bands by means of stochastic changes of intrinsic AGN power, and the corresponding power spectral density (PSD) should be similar to those of other type 1 AGNs. To examine the variability pattern of *Swift* light curves, we fit them with the CARMA code⁴ (Kelly et al. 2014) and derive the power spectral densities (PSDs). The CARMA code models the AGN stochastic variability using a Gaussian continuous-time autoregressive process, and uses two order parameters, p and q , to describe autoregressive coefficients and moving average coefficients of different stochastic processes. We determine p and q using the `choose_order` method in CARMA that selects the best model using the Akaike Information Criterion (see Section 3.5 in Kelly et al. 2014 for details). The fitting results and the PSD are shown in Figure 1. The PSD for the random walk model (i.e., $P(f) \propto f^{-2}$) is also displayed for comparison.

It is evident that the ten-year *Swift* light curves can be well fitted by a $p = 7$, $q = 2$ CARMA process (note that we only display the fitting result for the *UVM2* band but light curves in other bands can be also well fitted), including the occultation event reported in L15 (see our Section 4.4). Comparing the derived PSD shape with that of the random walk model, we find that the high-frequency PSD slope for WPVS 007 is consistent with -2 , i.e. the slope of the random walk process. The PSD then flattens at low frequencies, suggesting that the variabilities are damped at longer timescales (e.g., Kelly et al. 2009). Such a PSD shape is similar to those of other type 1 AGNs reported in previous studies (Kelly et al. 2009; MacLeod et al. 2010; Zu et al. 2013; Sun et al. 2015), and might be caused by the thermal fluctuations in the accretion disk (e.g., Kelly et al. 2009; Sun et al. 2018). Therefore, our results suggest that the intrinsic stochastic AGN variability being caused by a fluctuated accretion disk is able to well reproduce the observed *Swift* variability behavior, without the necessity to invoke other significant variable factors such as the change of dust extinction.

In addition, based on the 5100 Å luminosity ($\sim 3.5 \times 10^{43}$ erg s⁻¹ on Jun 2010), we estimate the inner-torus sublimation radius of WPVS 007 to be ~ 0.08 pc (Netzer 2015); the torus size at $\sim 8\text{--}13$ μm is estimated to be ~ 1 pc based on the relationship obtained through MIR-interferometry observations (see Figure 4 in Netzer 2015). Therefore, the torus size at *WISE* bands (~ 5 μm) might lie between $\sim 0.1\text{--}1$ pc.

Table 3. Thermal, viscous, and heating-cooling front timescales at *Swift* bands.

λ (Å)	t_{thermal} (yrs)	t_{viscous} (yrs)	t_{front} (yrs)
1929	0.011	1.68	0.14
2242	0.015	3.34	0.23
2609	0.021	6.48	0.37
3460	0.038	23.78	0.95
4384	0.061	68.75	2.05
5472	0.096	1769.30	4.14

Converting the distance into light crossing time, we expect the time delay between *WISE* and *Swift* variabilities to be ~ 600 days by roughly adopting $R_{4.6 \mu\text{m}} = 0.5$ pc. Although the sparse sampling of *WISE* observations does not allow us to robustly constrain the time delay, simply shifting *WISE* light curves by 600 days yields good agreement between *WISE* and *Swift* profiles, i.e., the rise and later decline of *WISE* data are consistent with the brightening and dimming of *Swift* data between MJD 56300 to MJD 56700, and MJD 56700 to MJD 57000, respectively (see the black crosses in Figure 1), thereby lending further support to the intrinsic nature of UV-optical variabilities.

4 DISCUSSION

Our analysis of archival *WISE* and *Swift* data suggests that the large-amplitude MIR variability, color variability, and UV-optical continuum flux variabilities discovered in the ten-year monitoring of WPVS 007 are most probably driven by the stochastic change of intrinsic luminosity, and variable extinction may play a minor role.

Following Section 3.2 (Page 108) of Kato et al. (2008), we calculate the timescales that are relevant to various intrinsic variability mechanisms at different wavelengths (radii): the thermal timescale t_{th} , which represents the timescale of thermal fluctuation of accretion disk; the viscous timescale t_{vis} , on which the global accretion rate changes; and the heating-cooling front timescale t_{front} , corresponding to the heating and cooling fronts propagating through an α disk (i.e., the viscosity in the accretion disk, which is crucial for driving the angular momentum of the accreted materials outward, is assumed to be αp , where α and p are the dimensionless viscous parameter and the total pressure, respectively; see Shakura & Sunyaev 1973). The results are listed in Table 3. Note that these values are derived under the assumption of a standard thin disk model for simplicity, since for $\lambda_{\text{Edd}} \sim 0.4$ as in WPVS 007, the disk remains geometrically thin at NUV/optical wavelengths. The local thermal fluctuation with $t_{\text{th}} \sim$ a few days produces the seed of short-timescale variability at a given radius (e.g., Sun et al. 2018). The t_{front} falls within the observed timescale, which makes it possible that the inner accretion disk could go through significant overall variability as the cooling and heating fronts propagate radially across an α disk, thus causing large variations at multiple wavelengths (e.g., Stern et al. 2018; Ross et al. 2018).

In the intrinsic luminosity variability scenario and within the radiatively-driven outflow framework, the outflow properties may display dramatic variability as the inci-

⁴ See https://github.com/brandonckelly/carma_pack.

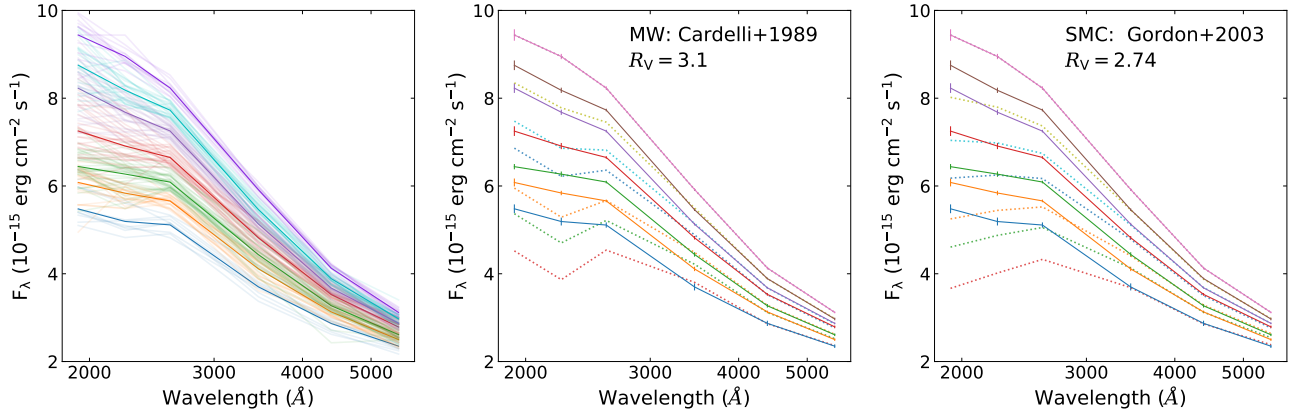


Figure 4. *Left:* *Swift* SEDs color-coded and sorted by their *UVW1* fluxes. The individual SEDs are shown in light colors while the average SEDs in seven *UVW1* flux bins are shown in bold curves. A clear bluer-when-brighter trend can be seen. *Middle:* The solid curves are the average *Swift* SEDs that are the same as those in the left panel. The dotted curves represent the SEDs derived from extinguishing the top SED (i.e., with the highest flux) using the Cardelli et al. 1989 MW extinction law with A_V ranging from 0 to 0.3. *Right:* Same as the middle panel, but using the Gordon et al. 2003 SMC extinction law. The pure variable extinction model fails to reproduce the observed color variability, since it significantly underestimates UV fluxes for a given A_V although the extinguished SEDs largely match the observed SEDs at longer wavelengths.

dent ionizing continuum changes. In the following sections, we investigate the BAL variability in WPVS 007, aiming at testing whether its behavior is consistent with being photoionization-driven, and try to put constraint on the outflow launch radius (e.g., Parker et al. 2017; Pinto et al. 2018).

4.1 Change of ionization state and BAL trough strength

The ionization parameter ($U \propto \frac{L}{n_{\text{H}}R^2}$) and ion column densities of the outflowing gas would change in response to the variable ionizing luminosity, resulting in the change of BAL strength. Using the best fit normalized BAL component (see the green curves in Figure 3), we calculate the equivalent width (EW) of C IV and Si IV BALs and list the results in Table 2. To qualitatively describe its relationship with luminosity, we calculate the concordance index C following Wang et al. (2015). C is assigned as +1 if BAL strength and bolometric luminosity vary in the same sign (i.e., both increasing or decreasing); otherwise, it is assigned as -1. The distribution of C for any two observations is shown in the bottom-right panel of Figure 2. All (most) epochs have $C = 1$ for C IV (Si IV) BAL, which suggests that the BAL and luminosity of WPVS 007 weaken and strengthen simultaneously.

Such a trend is different from what is typically observed in luminous quasars, for which the weakening of BAL trough is often accompanied with the brightening of continuum (e.g., Wang et al. 2015; He et al. 2017; Pinto et al. 2018). This may be explained by the different ionization states between WPVS 007 and quasars. For WPVS 007, Leighly et al. (2009) derived $N_{\text{H}} \sim 10^{23} \text{ cm}^{-2}$ (see also Grupe et al. 2013) and $\log U \gtrsim -0.3$ from the *FUSE* spectrum. The persistently weak N V line during 2010 to 2017 (see Figure 2) also suggests that it is in a lower ionization state compared with other luminous BAL quasars, possibly related to its low luminosity and X-ray weak nature (Grupe et al. 2007, 2008, 2013; Gibson et al. 2008). As shown in Figure 8 in He et al.

(2017), for $N_{\text{H}} \sim 10^{23} \text{ cm}^{-2}$, the column densities of C IV and Si IV ions reach the peaks at $\log U \sim 0$ and monotonically decrease at both sides. Therefore, for the low-ionization source WPVS 007 that lies on the left side of the peak of the N_{ion} vs. $\log U$ curve, the BAL strength and luminosity vary in a coordinated way.

4.2 Coordination between outflow velocity and AGN luminosity

We use the same concordance index method introduced in Section 4.1 to describe the relationship between BAL blue-shifted velocity and source luminosity. A similar coordinated correlation between bolometric luminosity and the “observed” maximum velocity can be also seen from Table 2 that V_{max} increases with increasing L_{bol} , including the faintest state in 1996 when no BALs were detected. For the C IV BALs, C is 1 for 14 out of 15 epochs, and the only exception happened at the two 2013 observations, at which the luminosity and velocity for the two epochs are actually very close to each other. While for the Si IV BALs, C is 1 for 80% (12/15) of the observations.

We note that if the change of apparent velocity is caused by a flowing structure randomly crossing our sightline (e.g., Hamann et al. 2008), equal probabilities of concordance (i.e., $C = 1$) and anti-concordance (i.e., $C = -1$) between V_{max} and L_{bol} should be expected in each pair of observations. Therefore, considering all observations, we should expect that half of the observations have $C = 1$ while the remaining have $C = -1$ (i.e., the distribution of C should follow a binomial distribution with a concordance probability of being 0.5). However, we find that 14 (12) out of 15 observations for C IV (Si IV) BALs have $C = 1$. Under the assumption of the moving-cloud scenario, the binomial probabilities for observing such events are only 0.0005 for C IV, and 0.014 for Si IV, respectively. Such low probabilities suggest that it is not very likely that the change of observed maximum velocity is caused by the transverse motion of obscuring clouds.

Instead, the coordinated correlation can be easily explained if the BAL variability is photoionization-driven (e.g., Hamann et al. 2011; FilizAk et al. 2012, 2013; Wang et al. 2015; He et al. 2017). As pointed out in Section 4.1, the C IV and Si IV column densities decrease when the source becomes fainter. For the high-velocity components of the outflow that typically have small absorption strengths and are more likely to vary (e.g., Capellupo et al. 2012), they would become weaker and disappear in the spectrum when the optical depth reduces, leading to the decrease of the “observed” maximum velocity when the source dims. The component with $V_{\max} > 10000 \text{ km s}^{-1}$ emerged for the C IV BAL in the Mar 2017 observation but no corresponding component was found for the Si IV BAL (see Figure 3) suggests that, the smaller optical depth of Si IV is responsible for the absence of the high-velocity component in the Si IV trough, owing to much smaller element abundance of Si IV compared to C IV. In addition, the increasing radiation pressure from Mar 2015 to Mar 2017 may also contribute to the increasing velocity, but current data do not allow measurement of the actual acceleration.

4.3 BAL velocity and outflow launch radius

If the outflows are launched radiatively, the large outflowing velocity may provide hints on its launch radius. To illustrate this, we express the motion equation of the radiatively-driven outflow as

$$\frac{v dv}{dR} = \frac{f_L L}{4\pi R^2 c m_p N_H} - \frac{GM_{\text{BH}}}{R^2}, \quad (1)$$

where v is the radial wind velocity, R is the radial distance, f_L is the fraction of continuum being absorbed or scattered in the wind, L is the bolometric luminosity, c is the speed of light, m_p is the mass of proton, M_{BH} is the black hole mass, respectively (Hamann 1998).

Integrating Eq. 1 from the launch radius to infinity yields the terminal velocity

$$v_\infty \approx 3200 R_l^{-1/2} \left(\frac{f_{0.1} L_{46}}{N_{22}} - 0.084 M_8 \right)^{1/2}, \quad (2)$$

where R_l is the launch radius in units of pc, $f_{0.1}$ is $f_L/0.1$, N_{22} is the column density relative to 10^{22} cm^{-2} , L_{46} is the bolometric luminosity relative to $10^{46} \text{ erg s}^{-1}$, and M_8 is the black hole mass in units of $10^8 M_\odot$, respectively.

The black hole mass was estimated to be $4.1 \times 10^6 M_\odot$ with a 0.43 dex uncertainty in L15. Using the observed maximum velocity as a proxy for terminal velocity and assuming $N_{22}/f_{0.1} \approx 2$ (Leighly et al. 2009), we obtain an average launch radius about $8 \times 10^{-4} \text{ pc}$ if the winds are produced in the dust-free region, consistent with Leighly et al. (2009). Note that the value of $N_{22}/f_{0.1}$ used here was calculated in Leighly et al. (2009) by approximately reconstructing the intrinsic X-ray to optical SED for WPVS 007 with the use of Mrk 335 and Mrk 493 SEDs as unattenuated templates. It is impossible to accurately measure this ratio during the 2010 to 2017 *HST* observations owing to the limited *HST* spectral coverage and weak X-ray signal. But we note that, adopting a larger (e.g., $N_{22}/f_{0.1} = 3$) or smaller (e.g., $N_{22}/f_{0.1} = 1$) ratio would obtain a launch radius about $4 \times 10^{-4} \text{ pc}$ or $2 \times 10^{-3} \text{ pc}$, which will not significantly influence our results.

We then calculate the evolution of wind velocity as a

function of acceleration time and radial distance with different initial conditions (L_{bol} , R_l , and $N_{22}/f_{0.1}$) using Eq. 1. The results are displayed in Figure 5. For a launch radius as small as $\sim 8 \times 10^{-4} \text{ pc}$, the outflow soon reaches its maximum velocity in a few tens of days, and an increase in velocity with luminosity can be clearly seen, which may also contribute to the coordination between outflow velocity and AGN luminosity, as discussed in Section 4.2.

According to the top panel of Figure 5, the outflow velocity reaches $\sim 10000 \text{ km s}^{-1}$ at a radial distance $\sim 0.01 \text{ pc}$, which is close to the torus sublimation radius estimated in Section 3.3. Therefore, the strongly blueshifted BAL features observed may be located far away from their launch radius and close to the torus, since the winds propagate and are accelerated outward (see Figure 5).

To test whether the outflows can be initially launched from the torus scale (Leighly et al. 2015), we assume that the torus can fully absorb the continuum (i.e., $f_L = 1.0$) to simulate the boosted radiation pressure caused by the presence of dust since dust has a much larger cross section compared with pure electron scattering. We adopt two column densities, i.e., the maximum ($N_H = 1.7 \times 10^{23} \text{ cm}^{-2}$) and minimum ($N_H = 2.8 \times 10^{22} \text{ cm}^{-2}$) column densities reported in Grupe et al. (2013) during 2005–2013 *Swift* observations, to calculate the launch radius. The derived R_l values are $3 \times 10^{-3} \text{ pc}$ and $3 \times 10^{-4} \text{ pc}$, respectively, which are all much smaller than the torus sublimation radius, thereby conflicting with our initial assumption that the outflows are launched in the torus. In addition, the fully absorbed scenario is also inconsistent with observations (Leighly et al. 2009); and more sophisticated calculations of radiation pressure implementing on dusty gas from the torus also indicated that the typical maximum outflow velocity is a few thousand km s^{-1} and hardly reaches $v > 10000 \text{ km s}^{-1}$, even if an enhanced dust to gas ratio is adopted for luminous dusty quasars (e.g., Ishibashi & Fabian 2016; Ishibashi et al. 2017). Therefore, we argue that the outflows in WPVS 007 may most probable to be launched in the region closer to the black hole, and the torus origin maybe less likely. But we note that since we only consider radiation pressure in our simple calculation, it is currently unclear how additional factors, such as the existence of magnetic field, would influence our result. Future numerical simulations are required to test whether outflows launched at a scale as large as the torus can reach the observed maximum velocity.

4.4 Comparison with previous analysis

L15 captured an occultation event lasting for ~ 60 days characterized by a continuous dimming of *UVM2* flux accompanied with the increase of $E(B-V)$. Through extensive color and timescale analyses, they concluded that such an event can be explained by variable extinction when different parts of a rotating torus moving into/out of our sightline. In addition, to explain the decreased BAL velocity during the occultation event, L15 proposed that the dusty gas is ablated from the rotating torus with variable scale height; and, the velocity of the outflowing gas decreases with increasing scale height (see Figure 5 and Section 3.4 in L15). Therefore, as the scale height increases during the occultation event, the torus may intercept our sightline, absorb the continuum flux and reduce the blue-shifted BAL velocity. As

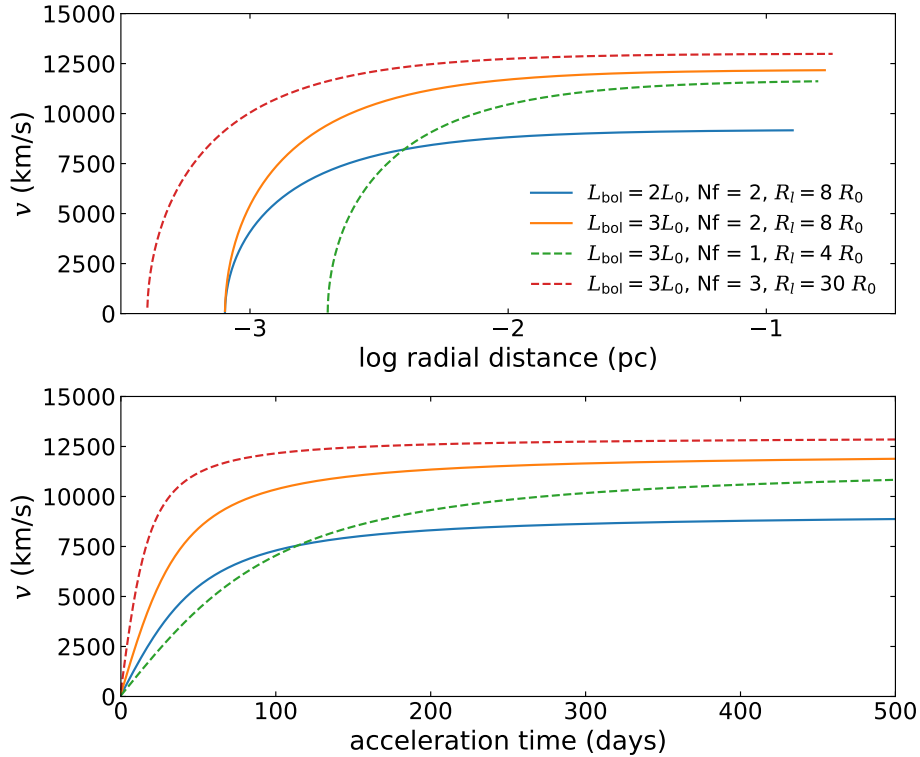


Figure 5. *Top:* Outflow radial velocity as a function of radial distance for different initial conditions calculated from Eq. 1 (where $L_0 = 10^{44} \text{ erg s}^{-1}$, $N_f = N_{22}/f_{0.1}$, and $R_0 = 10^{-4} \text{ pc}$). The initial conditions for curves in the same colors in both panels are the same. A clear correlation between the maximum outflow velocity and luminosity can be seen. For outflows launched in the inner region, e.g., $R_l = 0.0008 \text{ pc}$, the observed outflows that have $v \sim 10000 \text{ km s}^{-1}$ may be located far away from its birth region and lie close to the torus ($\sim 0.1 \text{ pc}$), since they propagate and are accelerated outward. *Bottom:* Outflow radial velocity as a function of acceleration time. For the launch radius as small as 0.0008 pc , the outflow soon reaches its maximum velocity in the observed timescales.

WPVS 007 emerges from the occultation event, a bluer and brighter SED with faster outflows will be revealed along our sightline again; this prediction is indeed consistent with the new *HST* observation in 2017.

However, we note that if outflows are launched close to the inner accretion disk as we conclude in Section 4.3, whether the variable-height torus rotates or not should not significantly affect the fast outflows, thus BALs. Alternatively, since we have already shown that the luminosity for this source must vary significantly, the UV-optical-MIR flux variabilities (including the occultation event, whose light curves can also be modeled by the AGN stochastic variability; see the lower-left panel of Figure 1), the coordinated BAL variabilities (both velocity and strength) with luminosities and the large outflow velocities can all be easily explained, if the variability is driven by the luminosity variations of the central engine and the outflows are launched close to the inner accretion disk.

5 CONCLUSION

WPVS 007, a low-luminosity NLS1, is noted for its unique spectral variability: being an X-ray bright, extremely soft AGN transforming into an X-ray weak source, the emergence of strong BALs compared with earlier observations, and dramatic outflows with V_{max} up to 14000 km s^{-1} given

its low luminosity. Therefore, this source can serve as an ideal laboratory to investigate the physical conditions of the extraordinary low-luminosity, NLS1-BAL systems.

To this end, we have intensively analyzed all the archival *WISE*, *Swift*, and *HST* observations of WPVS 007 in order to understand its peculiar variability nature and put important constraints on the driving mechanism of variable fast outflows in this rare object.

The observed significant MIR variability, the UV-optical color variabilities in the *Swift* bands that deviate from the prediction of pure dust attenuation models, and the fact that *Swift* light curves can be well fitted by the stochastic AGN variability model suggest that, the variability of intrinsic luminosity caused by the change of the inner accretion disk, rather than variable dust extinction, should be mainly responsible for these observed facts in WPVS 007.

We also test whether the variability behavior of BALs is consistent with being photoionization-driven and constrain the outflow launch radius. The ionization state of WPVS 007, traced by its weak N v line, might be much lower compared with other luminous BAL quasars, possibly related to its low luminosity and weak X-ray nature. At the low-ionization state, the C IV and Si IV column densities and luminosities are positively correlated. Owing to the reduction of optical depth as the WPVS 007 luminosity decreases, the C IV and Si IV BAL troughs become weaker; the high-velocity components of the outflow that typically have smaller absorption

strengths might be too weak to be detected, resulting in the coordination between the “observed” maximum velocity and its bolometric luminosity. Based on the radiatively-driven wind model, we estimate that the outflow launch radius might be as small as $\sim 8 \times 10^{-4}$ pc. However, a large-scale origin (e.g., the torus) cannot be fully excluded owing to the unknown effects from additional factors, e.g., magnetic field; future numerical simulations are required to test whether outflows launched at the torus scale can produce the observed maximum velocity.

6 ACKNOWLEDGMENTS

We thank Guilin Liu, Luming Sun and Guobin Mou for useful discussions. J.Y.L., M.Y.S., and Y.Q.X. acknowledge support from the NSFC (NSFC-11603022, NSFC-11473026, NSFC-11421303, NSFC-11890693), the 973 Program (2015CB857004), the CAS Frontier Science Key Research Program (QYZDJ-SSW-SLH006) and the K.C.Wong Education Foundation. M.Y.S. acknowledges support from the China Postdoctoral Science Foundation (2016M600485). T.G.W. and Z.C.H. acknowledge support from the 973 Program (2015CB857005) and the NSFC (NSFC116203021, NSFC-11703022, NSFC-11833007).

This publication makes use of data products from the *Wide-field Infrared Survey Explorer*, which is a joint project of the University of California, Los Angeles, and the Jet Propulsion Laboratory/California Institute of Technology, funded by the National Aeronautics and Space Administration. This publication makes use of data products from the *Near-Earth Object Wide-field Infrared Survey Explorer* (NEOWISE), which is a project of the Jet Propulsion Laboratory/California Institute of Technology. NEOWISE is funded by the National Aeronautics and Space Administration. This publication is based on observations made with the NASA/ESA Hubble Space Telescope, obtained from the data archive at the Space Telescope Science Institute. STScI is operated by the Association of Universities for Research in Astronomy, Inc. under NASA contract NAS 5-26555. We acknowledge the use of the public data from the Swift data archive and the UK Swift Science Data Center.

REFERENCES

- Begelman M. C., McKee C. F., Shields G. A., 1983, *ApJ*, **271**, 70
 Braitto V., et al., 2018, *MNRAS*, **479**, 3592
 Cai Z.-Y., Wang J.-X., Gu W.-M., Sun Y.-H., Wu M.-C., Huang X.-X., Chen X.-Y., 2016, *ApJ*, **826**, 7
 Cai Z.-Y., Wang J.-X., Zhu F.-F., Sun M.-Y., Gu W.-M., Cao X.-W., Yuan F., 2018, *ApJ*, **855**, 117
 Calzetti D., Armus L., Bohlin R. C., Kinney A. L., Koornneef J., Storchi-Bergmann T., 2000, *ApJ*, **533**, 682
 Capellupo D. M., Hamann F., Shields J. C., Rodríguez Hidalgo P., Barlow T. A., 2012, *MNRAS*, **422**, 3249
 Cardelli J. A., Clayton G. C., Mathis J. S., 1989, *ApJ*, **345**, 245
 Danekkar A., et al., 2018, *ApJ*, **853**, 165
 DeCicco D., Brandt W. N., Grier C. J., Paolillo M., Filiz Ak N., Schneider D. P., Trump J. R., 2018, *A&A*, **616**, A114
 Dexter J., Agol E., 2011, *ApJ*, **727**, L24
 Dunn J. P., et al., 2010, *ApJ*, **709**, 611
 Fabian A. C., 2012, *ARA&A*, **50**, 455
 FilizAk N., et al., 2012, *ApJ*, **757**, 114
 FilizAk N., et al., 2013, *ApJ*, **777**, 168
 Fitzpatrick E. L., 1999, *PASP*, **111**, 63
 Gehrels N., et al., 2004, *ApJ*, **611**, 1005
 Gibson R. R., Brandt W. N., Schneider D. P., 2008, *ApJ*, **685**, 773
 Gofford J., Reeves J. N., Tombesi F., Braitto V., Turner T. J., Miller L., Cappi M., 2013, *MNRAS*, **430**, 60
 Gofford J., et al., 2014, *ApJ*, **784**, 77
 Gordon K. D., Clayton G. C., Misselt K. A., Landolt A. U., Wolff M. J., 2003, *ApJ*, **594**, 279
 Grier C. J., et al., 2015, *ApJ*, **806**, 111
 Grier C. J., et al., 2016, *ApJ*, **824**, 130
 Grupe D., Beuerman K., Mannheim K., Thomas H.-C., Fink H. H., de Martino D., 1995, *A&A*, **300**, L21
 Grupe D., Schady P., Leighly K. M., Komossa S., O’Brien P. T., Nousek J. A., 2007, *AJ*, **133**, 1988
 Grupe D., Leighly K. M., Komossa S., 2008, *AJ*, **136**, 2343
 Grupe D., Komossa S., Scharwächter J., Dietrich M., Leighly K. M., Lucy A., Barlow B. N., 2013, *AJ*, **146**, 78
 Guo H., Gu M., 2016, *ApJ*, **822**, 26
 Hamann F., 1998, *ApJ*, **500**, 798
 Hamann F., Kaplan K. F., Rodríguez Hidalgo P., Prochaska J. X., Herbert-Fort S., 2008, *MNRAS*, **391**, L39
 Hamann F., Kanekar N., Prochaska J. X., Murphy M. T., Ellison S., Malec A. L., Milutinovic N., Ubachs W., 2011, *MNRAS*, **410**, 1957
 Harrison C. M., Alexander D. M., Mullaney J. R., Swinbank A. M., 2014, *MNRAS*, **441**, 3306
 He Z., Wang T., Zhou H., Bian W., Liu G., Yang C., Dou L., Sun L., 2017, *ApJS*, **229**, 22
 He Z., et al., 2019, *Nature Astronomy*, **3**, 265
 Ishibashi W., Fabian A. C., 2016, *MNRAS*, **463**, 1291
 Ishibashi W., Banerji M., Fabian A. C., 2017, *MNRAS*, **469**, 1496
 Jiang Y.-F., Stone J. M., Davis S. W., 2014, *ApJ*, **796**, 106
 Kato S., Fukue J., Mineshige S., 2008, *Black-Hole Accretion Disks — Towards a New Paradigm —*
 Kelly B. C., Bechtold J., Siemiginowska A., 2009, *ApJ*, **698**, 895
 Kelly B. C., Becker A. C., Sobolewska M., Siemiginowska A., Uttley P., 2014, *ApJ*, **788**, 33
 King A., Pounds K., 2015, *ARA&A*, **53**, 115
 Leighly K. M., Hamann F., Casebeer D. A., Grupe D., 2009, *ApJ*, **701**, 176
 Leighly K. M., Cooper E., Grupe D., Terndrup D. M., Komossa S., 2015, *ApJ*, **809**, L13
 MacLeod C. L., et al., 2010, *ApJ*, **721**, 1014
 Mainzer A., et al., 2014, *ApJ*, **784**, 110
 Matzeu G. A., Reeves J. N., Nardini E., Braitto V., Costa M. T., Tombesi F., Gofford J., 2016, *MNRAS*, **458**, 1311
 Matzeu G. A., Reeves J. N., Braitto V., Nardini E., McLaughlin D. E., Lobban A. P., Tombesi F., Costa M. T., 2017, *MNRAS*, **472**, L15
 Matzeu G. A., et al., 2019, *MNRAS*, **483**, 2836
 McGraw S. M., Shields J. C., Hamann F. W., Capellupo D. M., Herbst H., 2018, *MNRAS*, **475**, 585
 Netzer H., 2015, *ARA&A*, **53**, 365
 O’Donnell J. E., 1994, *ApJ*, **422**, 158
 Ohsuga K., Mineshige S., Mori M., Kato Y., 2009, *PASJ*, **61**, L7
 Parker M. L., et al., 2017, *Nature*, **543**, 83
 Pinto C., et al., 2018, *MNRAS*, **476**, 1021
 Pounds K. A., Reeves J. N., King A. R., Page K. L., O’Brien P. T., Turner M. J. L., 2003, *MNRAS*, **345**, 705
 Proga D., Kallman T. R., 2004, *ApJ*, **616**, 688
 Proga D., Stone J. M., Kallman T. R., 2000, *ApJ*, **543**, 686
 Reeves J. N., O’Brien P. T., Ward M. J., 2003, *ApJ*, **593**, L65
 Rogerson J. A., Hall P. B., Rodríguez Hidalgo P., Pirkola P., Brandt W. N., Filiz Ak N., 2016, *MNRAS*, **457**, 405
 Ross N. P., et al., 2018, *MNRAS*, **480**, 4468

- Ruan J. J., Anderson S. F., Dexter J., Agol E., 2014, *ApJ*, **783**, 105
- Runnoe J. C., Brotherton M. S., Shang Z., 2012, *MNRAS*, **422**, 478
- Schlegel D. J., Finkbeiner D. P., Davis M., 1998, *ApJ*, **500**, 525
- Shakura N. I., Sunyaev R. A., 1973, *A&A*, **24**, 337
- Sheng Z., Wang T., Jiang N., Yang C., Yan L., Dou L., Peng B., 2017, *ApJ*, **846**, L7
- Stern D., et al., 2018, *ApJ*, **864**, 27
- Sun M., et al., 2015, *ApJ*, **811**, 42
- Sun M., Xue Y., Wang J., Cai Z., Guo H., 2018, *ApJ*, **866**, 74
- Tombesi F., Sambruna R. M., Reeves J. N., Braitto V., Ballo L., Gofford J., Cappi M., Mushotzky R. F., 2010, *ApJ*, **719**, 700
- Vaughan S., Edelson R., Warwick R. S., 2004, *MNRAS*, **349**, L1
- Wang T., Yang C., Wang H., Ferland G., 2015, *ApJ*, **814**, 150
- Wright E. L., et al., 2010, *AJ*, **140**, 1868
- Zu Y., Kochanek C. S., Kozłowski S., Udalski A., 2013, *ApJ*, **765**, 106

This paper has been typeset from a $\text{\TeX}/\text{\LaTeX}$ file prepared by the author.